

Hysteresis of Charge Tunneling in Assemblies of Carboxylic Acid-Modified Gold Nanoparticles

Matteo Biancardo,^{†,‡} Aidan J. Quinn,[‡] Liam Floyd,[‡] Paula M. Mendes,[§] Simon S. Briggs,[§] Jon A. Preece,[§] Carlo A. Bignozzi,[†] and Gareth Redmond^{*,‡}

Department of Chemistry, University of Ferrara, Via Luigi Borsari, 46, 44100 Ferrara, Italy, Nanotechnology Group, Tyndall National Institute, Lee Maltings, Prospect Row, Cork, Ireland, and School of Chemistry, University of Birmingham, Birmingham, B15 2TT, United Kingdom

Received: November 18, 2004; In Final Form: February 10, 2005

We report on charge transport measurements through laterally contacted assemblies of Au nanoparticles capped with 11-mercaptoundecanoic acid ligands. Both alternating- and direct-current data indicate that although the nanoparticles behave as electrically isolated metallic islands, there is a significant influence from the nanoparticle environment, indicating the existence of a slow reorganization process linked to charge transport. On the basis of the observation of temperature-dependent hysteresis of charge tunneling, we propose that this process is due to proton transfer between the carboxylic acid tails of the ligands.

Introduction

Assemblies of organically passivated nanoparticles can exhibit collective behavior if individual nanoparticles couple to neighbors. Arrays of such nanoparticles therefore offer the promise of artificial atom solids with novel electronic and optical properties.^{1–8} These properties could be derived from the size-dependent electronic characteristics of the nanoparticle cores,^{1–3} the internanoparticle coupling mechanisms,^{3,7–9} and the chemical nature of the protecting ligand.^{1,7} Although most reports to date have focused on alkanethiolate-protected nanoparticles, functionalization of the protective capping layer has enabled recent progress in the synthesis and characterization of assemblies of water-soluble nanoparticles, passivated with, for example, alkylthiolated carboxylic acid ligands.^{10–17} This offers the possibility of multidimensional hydrogen-bonded nanoparticle architectures or hybrid nanoparticle-supramolecular assemblies.^{10,12,16,18,19} The role of ligands, solvent, and other species in these assemblies and their effects on the resulting charge transport characteristics of these nanoparticle arrays is currently the subject of intense research interest with reports of ion-dependent shifts of the nanoparticle charging potential,¹¹ rectification of quantized nanoparticle charging in aqueous electrolyte solutions,¹⁴ and increased sensitivity to the gaseous ambient.¹⁷ However, development of a unified picture of electron transport in functionalized nanoparticle assemblies remains a significant challenge in the area of nanoscale charge transfer.²⁰

From a technological viewpoint, the influence of the local environment, and of mobile ions in particular, on the electronic properties of devices incorporating nanoparticles, nanowires, or nanotubes is also attracting considerable attention since it has become apparent that nanoscale devices can be extremely sensitive to the local charge environment because of their large relative surface area.^{21–23} This environmental sensitivity presents device fabrication challenges in terms of performance, yield, or reproducible operation because of hysteresis effects and

highlights the importance of device passivation for future nanoelectronic applications. However, this sensitivity can also be exploited as the basis for nanoscale field-effect logic, sensor or memory devices based on reversible charge manipulation,^{24–28} where reconfiguration of mobile charges in the local environment results in electrostatic gating of device conductance.

In this work, we investigate nanoparticle-environment coupling by probing charge transport in laterally contacted self-assembled arrays of carboxylic acid-modified gold nanoparticle devices with channel lengths ranging from 50 nm to 8 μ m. Despite the metallic luster of the nanoparticle films, charge transport data from both alternating-current (AC) and direct-current (DC) measurements indicate that the nanoparticles behave as electrically isolated metallic islands separated by tunnel barriers. The AC and DC data also indicate a significant influence arising from the local nanoparticle environment, which we propose is due to proton transfer between the carboxylic acid tails of the ligands. In the Coulomb Blockade regime, that is, at sufficiently low temperatures, this process can be exploited for demonstration of two-terminal memory effects, highlighting the possibilities for development of hybrid nanoparticle-molecular devices for future memory or sensor applications.

Experimental Section

Gold nanoparticles passivated with 11-mercaptoundecanoic acid (Au:MUA) were synthesized using the Brust method.²⁹ All solvents were degassed with Ar prior to use and were maintained under an Ar atmosphere. Deionized water (Millipore Q, > 18 M Ω cm) was used for all aqueous solutions. An aqueous solution of NaBH₄ (5 mM) was added to a vigorously stirred toluene solution of HAuCl₄ (5 mM) in the presence of tetraoctylammonium bromide (TOAB, 1 mM). A rapid color change from orange to red-brown was observed. The solution was stirred for a further 2 h. Following removal of the toluene in vacuo and resuspension of the nanoparticles in CH₂Cl₂, subsequent addition of MUA in CH₂Cl₂ resulted in immediate precipitation of the nanoparticles. The nanoparticle dispersion was purified by repeated cycles of resuspension in H₂O, precipitation with 50:50 CH₃OH:CH₂Cl₂, and then centrifugation to collect the

* Corresponding author. E-mail: gareth.redmond@tyndall.ie.

[†] University of Ferrara.

[‡] Tyndall National Institute.

[§] University of Birmingham.

precipitant. Transmission electron microscopy (TEM) images of the gold nanoparticles were collected on a Philips CM20 transmission electron microscope operating at 200 kV. Samples were prepared by slow evaporation of one drop of a dilute solution of the nanoparticles on a carbon-coated copper mesh grid. Histogram analysis of TEM images containing several hundred nanoparticles yielded a mean core diameter of 5.9 nm and a size dispersion, $\sigma = 20\%$.

For measurements of AC electrical characteristics of nanoparticle assemblies, interdigitated microelectrodes were fabricated on thermally oxidized silicon wafer chips using optical lithography, metal evaporation (Cr 10 nm/Au 100 nm), and lift-off. For DC measurements, paired gold finger electrodes (80 nm in width) with interelectrode gaps of ~ 50 nm were fabricated on oxidized Si wafer chips using electron beam lithography, metal evaporation (Cr 5 nm/Au 25 nm), and lift-off. Nanoparticle assemblies were formed between the micro- and nano-electrodes by dropping $\sim 5 \mu\text{L}$ of a $20 \mu\text{M}$ nanoparticle solution (13.2 mg of nanoparticles in $480 \mu\text{L}$ EtOH + $40 \mu\text{L}$ H₂O) onto each electrode array under ambient conditions and allowing the chip to dry in air for 1 h. Optical images were acquired using a microscope (Bausch & Lomb Micro Zoom II) coupled to a digital camera (JVC). SEM data were acquired using a field-emission SEM (JSM-6700F, JEOL UK Ltd.) operating at beam voltages between 1 and 10 kV.

Room-temperature impedance spectroscopy data ($Z_{\text{meas}}(\omega)$) were acquired for nanoparticle arrays self-assembled between interdigitated electrodes (interelectrode gaps of either $4 \mu\text{m}$ or $8 \mu\text{m}$) on oxidized silicon substrates contacted using a probe station (PML-8000, Wentworth Labs, United Kingdom) interfaced to a precision LCR meter (HP 4284A, Agilent Technologies, United Kingdom) for frequencies (f) from 20 Hz to 800 kHz ($\omega = 2\pi f$). Blank chips were also measured to allow the contribution of the electrodes to the measured impedance data to be de-embedded. By treating the contribution of the electrodes ($Z_{\text{blank}}(\omega)$) as an impedance in parallel to the impedance of the nanoparticle assembly ($Z(\omega)$), the assembly impedance can be extracted: $Z(\omega)^{-1} = Z_{\text{meas}}(\omega)^{-1} - Z_{\text{blank}}(\omega)^{-1}$. Following instrument calibration, control measurements were performed on simple test circuits (a surface-mount 100Ω resistor in series with a 22 pF capacitor). As expected from the instrument specifications, the extremely large impedances presented at low frequencies ($f < 40 \text{ kHz}$) could not be accurately measured, and therefore data acquired at these frequencies are not included.⁴ DC electrical measurements of nanoparticle devices (with interelectrode gaps $\sim 50 \text{ nm}$) were performed using a semiconductor parameter analyzer (HP4156A, Agilent Technologies, United Kingdom), with voltage resolution $< 100 \mu\text{V}$ and current resolution $< 100 \text{ fA}$, programmed using HP VEE 6.0. For room-temperature measurements, electrode chips were contacted using a probe station. For variable-temperature measurements (3–400 K), chips were mounted in leadless chip carriers, wire-bonded, and inserted into a liquid helium bath cryostat (Spectrostat, Oxford Instruments, United Kingdom).

Results and Discussion

Figure 1 shows SEM images of a typical set of measurement electrodes fabricated on an oxidized Si chip and optical micrographs of the electrodes before and after deposition of the nanoparticle layer. The deposited and dried Au:MUA nanoparticle film displays a homogeneous metallic luster across the entire chip surface (see Figure 1c) similar to that observed in highly compressed Langmuir monolayers of propanethiol-capped Ag nanoparticles (3.5-nm diameter)³ and for multilayer

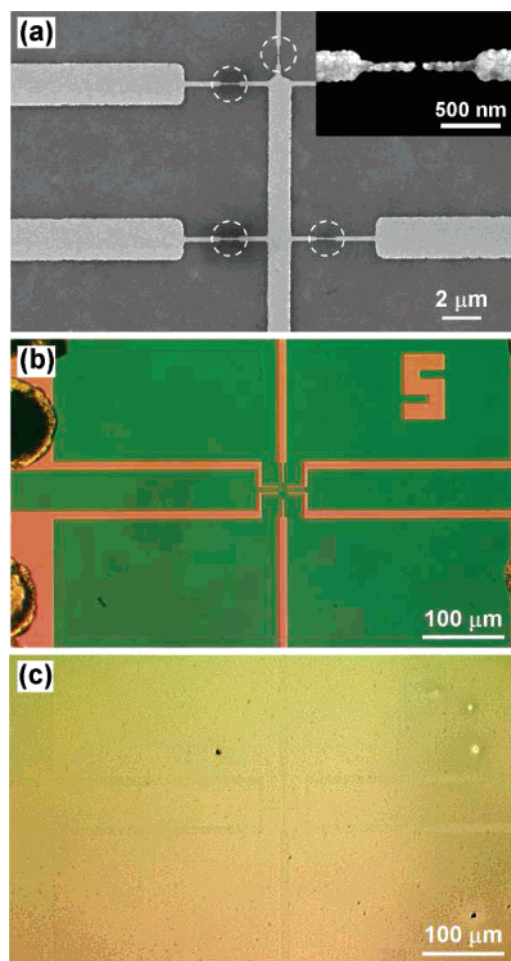


Figure 1. (a) Scanning electron microscopy image of a typical set of measurement electrodes on an oxidized Si chip substrate. Dashed circles indicate the individual sets of paired finger electrodes. Inset: High-magnification image showing a single electrode pair (interelectrode gap $\sim 50 \text{ nm}$). (b) Lower magnification optical micrograph of the electrodes. (c) Optical micrograph of the electrodes shown in b after self-assembly of a layer of MUA-terminated gold (Au:MUA) nanoparticles. The uniform metallic luster is evident.

assemblies of dithiol^{5,6} and bis-dithiocarbamate-linked Au nanoparticles.⁷ In these reports, the mean internanoparticle separation (s) was calculated to be $< 0.5 \text{ nm}$ for the compressed arrays³ and the assemblies linked with short (C_3) alkane chains.⁶ For assemblies linked with C_9 -dithiol⁵ and bis-dithiocarbamate molecules,⁷ s was calculated to be $\sim 1 \text{ nm}$. SEM data obtained for nanoparticle films (not shown) indicate that the films adhere to the substrate, forming compact assemblies with finite nanoscale packing disorder, arising from the nanoparticle size dispersion and the deposition method.^{8,9,30}

We have utilized room-temperature impedance spectroscopy to probe the low-frequency charge transport mechanisms of micron-scale assemblies of Au:MUA nanoparticles. Figure 2 (inset) shows a complex-plane plot of measured impedance data for a typical nanoparticle array device (interelectrode gap $\sim 8 \mu\text{m}$) from 40 to 800 kHz. The data appear as a skewed arc, highlighting two important points: First, the assembly behaves as a network of parallel resistor-capacitor (RC) elements, indicating that the nanoparticle array is an insulator. There is no inductive component in the impedance data, which would be expected for strong (i.e., metallic) internanoparticle coupling, despite the metallic sheen of the deposited arrays.³ Therefore, the assembly can be thought of as an array of discrete metal islands separated by insulating tunnel barriers. Second, the fact

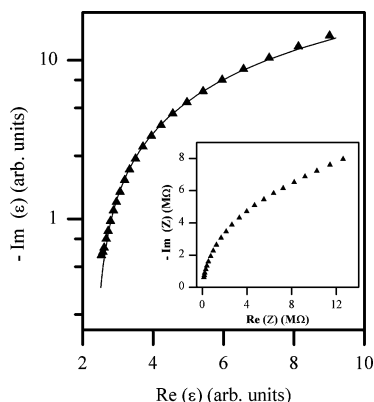


Figure 2. Semilog plot of imaginary vs real components of the dielectric permittivity (ϵ) extracted from measured room-temperature impedance data (inset) for a Au:MUA nanoparticle array self-assembled between interdigitated electrodes (interelectrode gap: 8 μm). The solid line in the main panel shows the fit to a Cole–Davidson model for a distribution of relaxation times centered around $\tau = 1.1$ ms.

that the data cannot be described by an arc of a single semicircle suggests a distribution of RC relaxation times in the assembly, consistent with the finite nanoparticle size dispersion, $\sigma = 20\%$. In the present case, the data are best represented in terms of the complex dielectric permittivity, $\epsilon(\omega) = (i\omega C_0)^{-1} Z(\omega)^{-1}$, where C_0 is a constant. For a system with a distribution of relaxation times, the data should follow a Cole–Davidson form: $\epsilon(\omega) = \epsilon_\infty + (\epsilon_s - \epsilon_\infty)/[1 + (i\omega\tau)^\gamma]$, where ϵ_s is the low-frequency permittivity, ϵ_∞ is the high-frequency permittivity, τ is the mean relaxation time, and the exponent γ is related to the standard deviation of the distribution of relaxation times.³¹ Figure 2 shows a semilog complex-plane plot of $\epsilon(\omega)$ for the device with impedance data shown in the inset. The data are well-described by a fit to the Cole–Davidson equation for $\omega\tau \gg 1$. For all such measured devices, data fits yield relaxation times in the range 0.4 ms $< \tau < 1.1$ ms and exponents of 0.71 $< \gamma < 0.72$. The extracted values of γ indicate a reasonably narrow range of relaxation times, consistent with the nanoparticle size dispersion measured by TEM ($\sigma = 20\%$).

The magnitude of τ suggests either a large internanoparticle separation or the existence of a slow environment reorganization process associated with charge transport within the array. Considering the internanoparticle separation, it might be intuitively proposed that the assembly consists of nanoparticle cores separated by extended thiolated C₁₀COOH ligands, such that the mean internanoparticle separation (s) is greater than twice the length of the free ligand. However, charge transport data for a series of “network polymer” assemblies of Au nanoparticles (1.6-nm diameter) capped by mixed monolayers of alkanethiols (C₄–C₁₂) and thiolated (C₆–C₁₆) carboxylic acid ligands, and linked by carboxylate/metal ion/carboxylate bridges,^{16,17} contradict this simplistic picture. The measurements point to the inherent flexibility of the MUA ligands, even when linked by metal ions, such that the MUA ligands fold up and the mean internanoparticle separation is determined primarily by the length of the alkanethiol ligand.¹⁷ In addition to these reports, the metallic luster observed for our Au:MUA nanoparticle films (Figure 1) is consistent with a relatively small internanoparticle separation ($s \sim 1$ nm).^{3–7} Therefore, the values for τ extracted from the impedance spectroscopy data (Figure 2) suggest the existence of a slow environmental process associated with charge transport, rather than a low-electron-transfer rate because of a large mean internanoparticle separation. Possible candidates for such a process include reorganization of the MUA ligands or ionic motion linked to proton

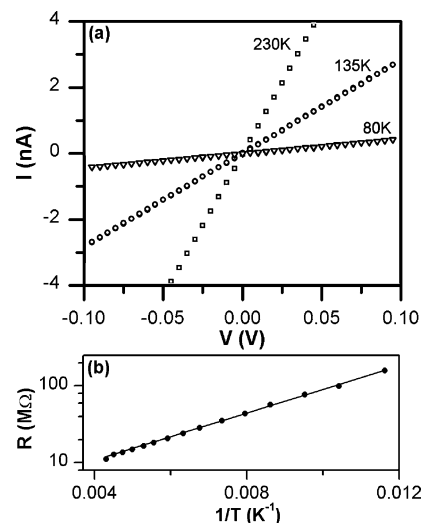


Figure 3. (a) Variable-temperature current–voltage (I – V) characteristics for a typical Au:MUA nanoparticle array device (interelectrode gap ~ 50 nm). (b) Semilog plot of low bias resistance (R) vs inverse temperature ($1/T$). Data (circles) are well fit by an activation model (solid line) for $k_B T < E_c$ ($E_c = 30$ meV).

exchange between the carboxylic acid tails of the ligands. Concerning the former proposal, values for τ extracted from measured data are several decades larger than values associated with electronic or vibrational transitions,³² which seems to rule out ligand reorganization.

Concerning the latter proposal, variable-temperature DC electrical characterization was employed to further probe the charge transport mechanisms in small arrays of Au:MUA nanoparticles, that is, where the shortest conducting path through a given assembly contained < 10 nanoparticles. Room-temperature current–voltage (I – V) characteristics of assemblies deposited between electrodes (with interelectrode gaps ~ 50 nm) exhibited ohmic behavior at low bias, with measured device resistances (R) in the range 10–50 M Ω . Taking the assembly dimensions as 50 \times 80 \times 30 nm³, that is, assuming the nanoparticles completely fill the interelectrode gap, the corresponding device resistivities (ρ) lie in the range $\rho \sim 0.5$ –2.5 Ωm . Figure 3a shows the measured low-bias I – V characteristics versus temperature (T) for a typical device. For all measured devices, the low-bias I – V data are symmetric and no hysteresis is observed in the measured current as the bias voltage is swept (V : 0 \rightarrow V_{max} \rightarrow 0 \rightarrow $-V_{\text{max}}$ \rightarrow 0). R increases monotonically with decreasing T , consistent with the Neugebauer–Webb model for tunnel transport through an array of isolated, size-similar, metallic islands, where the carrier density is activated: $R \propto \exp(E_c/k_B T)$ for $k_B T < E_c$, where E_c is the island charging energy and k_B is the Boltzmann constant.⁸ Figure 3b presents a semilog plot of R versus $1/T$ for the device with I – V data shown in Figure 3a demonstrating that the device exhibits activated behavior in the temperature range 80–230 K. Therefore, both the DC and AC data provide a consistent picture of tunnel transport through an array of discrete metal islands, separated by insulating barriers. For all such measured devices, fits to the DC data yield activation energies for nanoparticle charging in the range 30 meV $< E_c < 32$ meV. These values are somewhat larger than extracted values for E_c obtained from R versus T data measured for multilayer assemblies of 1,9-nonanedithiol-linked 6-nm diameter Au nanoparticles ($E_c = 20 \pm 2$ meV).⁵ In this regard, E_c is related to the total nanoparticle capacitance (C_Σ) via $E_c = e^2/2C_\Sigma$. This suggests a smaller effective capacitance for the MUA-passivated nanoparticles relative to the dithiol-linked nanoparticles. This reduction in

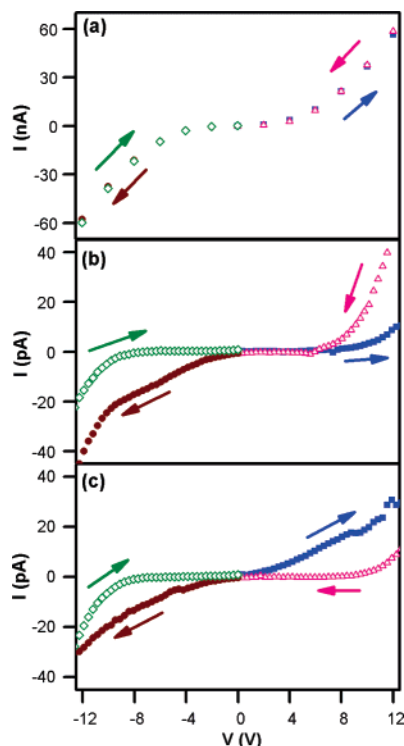


Figure 4. Measured low-temperature I – V characteristics for the device with I – V data shown in Figure 3. The arrows indicate the direction of the successive voltage sweeps: $0 \rightarrow +V_{\max}$ (+35 V), $+V_{\max} \rightarrow 0$, $0 \rightarrow -V_{\max}$ (–35 V), $-V_{\max} \rightarrow 0$. (a) $T = 38$ K: No hysteresis observed. (b) $T = 4$ K: First measured I – V characteristic. (c) $T = 4$ K: Second I – V showing reproducible hysteresis at both positive and negative bias.

C_{Σ} could be due to fewer nearest neighbors in the Au:MUA nanoparticle assembly, a smaller effective dielectric constant for the MUA ligand environment relative to the dithiols, or reduced internanoparticle separation in the dithiol assembly, perhaps because of ligand intercalation.

Since the nanoparticle size dispersion ($\sigma = 20\%$) is slightly larger than the accepted limit for monodisperse particles ($\sigma \leq 15\%$), one could argue that the R versus T data could also be described using the Abeles model first derived for arrays of polydisperse metal islands in insulating matrixes, $R \propto \exp(2[E^*/k_B T]^{1/2})$, where E^* represents the mean charging energy.³³ However, fitting the data to this model yields $E^* \sim 105$ meV, a value considerably larger than that expected for ~ 6 nm diameter nanoparticles.⁵ Simulations by Black and co-workers show that the R versus T characteristics for assemblies of polydisperse nanoparticles only begin to deviate from activated transport ($R \propto \exp[1/T]$) for nanoparticle size dispersions, $\sigma > 15\%$.³⁴ For $\sigma = 20\%$, their simulations show a deviation from activated transport only at very low temperatures ($T < 30$ K). Further, they propose that such R versus T data should tend toward the Abeles form ($R \propto \exp[1/T]^{1/2}$) for $\sigma > 50\%$. Therefore, we are confident that the activation model provides an accurate interpretation of the data.

Concerning low-temperature I – V data, pronounced nonlinearity appears in the I – V curve near zero bias for $T < 40$ K; see Figure 4a. Complete current suppression is observed at low bias ($R > 10$ G Ω), that is, a finite threshold voltage, V_T , is required to pass current through the array.^{8,9,30} This threshold voltage corresponds to the sum of the voltages required to lift the single-electron Coulomb Blockade across each of the individual nanocrystals in the most favorable current path through the array. For the device with I – V data shown in Figure

3 and Figure 4a, a $V_T \sim 2$ V may be observed at $T = 38$ K. The I – V characteristics are symmetric and no hysteresis is observed even at high bias (35 V). However, lowering the temperature even further has a dramatic effect on the charge transport characteristics. Figure 4b shows the first I – V measurement for this device at $T = 4$ K. The first part of the sweep ($0 \text{ V} \rightarrow 35 \text{ V}$) shows complete current suppression below $V_T = 8$ V. Clear hysteresis is observed on the return sweep ($35 \text{ V} \rightarrow 0 \text{ V}$) with an accompanying shift in the threshold voltage, $V_T = 6$ V (advanced hysteresis). The subsequent negative sweeps ($0 \text{ V} \rightarrow -35 \text{ V} \rightarrow 0 \text{ V}$) and the second measurement at 4 K for the device (Figure 4c) also show hysteretic behavior but with a reproducible *retarded* hysteresis pattern: Small values of V_T (~ 2 V) for sweeps from $0 \rightarrow \pm 35 \text{ V}$, with a shift to larger values of V_T (~ 8 V) for the return sweeps. It appears that the first sweep at positive voltage (Figure 4b: $0 \text{ V} \rightarrow 35 \text{ V} \rightarrow 0 \text{ V}$) conditions the device.²⁷ The subsequent sweeps (Figure 4b: $0 \text{ V} \rightarrow -35 \text{ V} \rightarrow 0 \text{ V}$ and Figure 4c) demonstrate reproducible memory effects.

Threshold voltage shifts, resulting from electrostatic gating of device conduction because of the presence of background charges, are well-known in conventional metal–oxide–semiconductor (MOS) devices³⁵ and are also a general feature of single electron devices, which are based on the controllable transfer of single electrons between small conducting islands.³⁶ Similar behavior has also been observed in nanotube^{22–26} and nanowire devices.^{27,28} Such shifts present challenges for logic device applications but offer opportunities for nanoscale sensors or memory devices. Concerning the origin of the hysteretic behavior observed in our devices, the maximum electric field employed is estimated to be $E_{\max} \sim 0.7$ V/nm (corresponding to a bias of 35 V across a 50-nm gap), which is below the breakdown field for SiO_2 (≥ 1 V/nm). E_{\max} is close to the accepted threshold for Fowler–Nordheim tunneling through SiO_2 ,³⁷ so electron injection into the oxide layer under the nanoparticles is possible at high bias. However, since hysteresis was never observed in measured I – V data for our devices at temperatures at or above 38 K and at applied biases up to 35 V, the low-temperature hysteresis cannot be explained simply in terms of electric-field-induced charge trapping within the substrate oxide.

Hysteresis may also be associated with the existence of an environment reorganization process, coupled to charge transport within the active region of a device, for example, electric-field-induced migration of mobile ions. Assuming that the process we observe is activated, that is, $\tau(T) \propto \exp(E_{\tau}/k_B T)$, the room-temperature relaxation time $\tau(300 \text{ K}) \sim 1$ ms, extracted from fitting of the AC data shown in Figure 2, should increase as the temperature is lowered, and hysteresis should appear in the DC I – V data at temperatures where the relaxation time is significantly larger than the time scale of a typical I – V sweep.³⁸ Since hysteresis was observed in charge tunneling data at $T = 4$ K but not at $T = 38$ K, this suggests that $E_{\tau}/k_B \sim 38$ K ($E_{\tau} \sim 3.3$ meV). In this regard, we can exclude contributions to hysteresis from ionic motion through the underlying oxide layer since measurements on ion mobility in MOS devices yielded activation energies orders of magnitude greater than our estimates: ~ 970 meV for Li and ~ 1400 meV for Na.³⁹ Similarly, studies on Si/SiO₂/Si memory devices revealed activation energies ~ 800 meV for proton mobility in the buried oxide layer.⁴⁰ By comparison, low-temperature NMR studies of proton transfer in single crystals of benzoic acid revealed an activated spin–lattice relaxation time, with $E_{\tau}/k_B = 88$ K ($E_{\tau} \sim 7.6$ meV), comparable to our estimate.⁴¹

Therefore, both the AC and DC data suggest that the environmental process causing the measured hysteresis is due to ionic motion within the nanoparticle array, likely to be proton exchange between the carboxylic acid tail groups of the MUA ligands, since neighboring nanoparticles are probably interconnected by hydrogen bonds, either directly between the $-\text{COOH}$ groups or via bridging water molecules.^{10,12} The water molecules could originate from the laboratory atmosphere, unevaporated solvent, or water adsorbed on the silicon oxide substrate. These results indicate that the local ionic environment is indeed a key factor governing the electronic properties of nanoscale devices incorporating nanoparticles, as previously observed for carbon nanotube devices.^{21–26} Similar two-terminal memory effects have been demonstrated on nanowires functionalized with redox-active molecules,^{27,28} where a source-drain voltage pulse was employed to inject charge onto the molecules and subsequent I – V sweeps of the nanowire showed hysteresis resulting from this electrostatic gating. Importantly, such two-terminal configurations allow addressing of individual nanodevices and can be utilized in integrated or parallel device formats without the need for a third (gate) terminal.²⁷

In conclusion, we have fabricated laterally contacted self-assembled arrays of carboxylic-acid-terminated nanoparticles with channel lengths ranging from 50 nm to 8 μm . Room-temperature AC data indicate that, despite their metallic luster, the nanoparticle assemblies behave as networks of RC elements, that is, metallic islands separated by tunnel barriers. Fits to the data yield relaxation times ~ 1 ms, suggesting the existence of a slow environment reorganization process associated with nanoparticle charging. Variable-temperature DC charge transport data confirm that the nanoparticles behave as electrically isolated metallic islands, and reproducible low-temperature memory effects provide further evidence of the environment reorganization. We propose that this reorganization is due to proton transfer between the carboxylic acid tail groups of the ligands. Similar hysteretic behavior linked to the presence of local ions has previously been observed in two-terminal nanowire devices. This highlights the possibilities for development of integrated nanoparticle-based sensor or memory devices through tuning of ligand chemistry.

Acknowledgment. The authors thank Gianluca De Marzi for SEM imaging and Oliver Harnack of SONY Europe for assistance with electrode fabrication. This work was supported by the EU under the “MicroNano” project (HPRN-CT-2000-00028) and by the HEA PRTL Nanoscience Initiative.

References and Notes

- Templeton, A. C.; Wuelfing, W. P.; Murray, R. W. *Acc. Chem. Res.* **2000**, *33*, 11465. Murray, C. B.; Kagan, C. R.; Bawendi, M. G. *Annu. Rev. Mater. Sci.* **2000**, *30*, 545.
- Terrill, R. H.; Postlethwaite, T. A.; Chen, C. H.; Poon, C. D.; Terzis, A.; Chen, A. D.; Hutchison, J. E.; Clark, M. R.; Wignall, G.; Londono, J. D.; Superfine, R.; Falvo, M.; Johnson, C. S.; Samulski, E. T.; Murray, R. W. *J. Am. Chem. Soc.* **1995**, *117*, 12537.
- Andres, R. P.; Bielefeld, J. D.; Henderson, J. I.; Janes, D. B.; Kolagunta, V. R.; Kubiak, C. P.; Mahoney, W.; Osifchin, R. G. *Science* **1996**, *273*, 1690. Feldheim, D. L.; Grabar, K. C.; Natan, M. J.; Mallouk, T. E. *J. Am. Chem. Soc.* **1996**, *118*, 7640. Ingram, R. S.; Hostetler, M. J.; Murray, R. W.; Schaff, T. G.; Khoury, J. T.; Whetten, R. L.; Bigioni, T. P.; Guthrie, D. K.; First, P. N. *J. Am. Chem. Soc.* **1997**, *119*, 9279.
- Collier, C. P.; Saykally, R. J.; Shiang, J. J.; Henrichs, S. E.; Heath, J. R. *Science* **1997**, *277*, 1978. Markovich, G.; Collier, C. P.; Heath, J. R. *Phys. Rev. Lett.* **1998**, *80*, 3807. Beverly, K. C.; Sampaio, J. F.; Heath, J. R. *J. Phys. Chem. B* **2002**, *106*, 2131.
- Brust, M.; Bethell, D.; Kiely, C. J.; Schiffrin, D. J. *Langmuir* **1998**, *14*, 5425.
- Brust, M.; Kiely, C. J. *Colloids Surf., A* **2002**, *202*, 175.
- Wessels, J. M.; Nothofer, H.-G.; Ford, W. E.; von Wrochem, F.; Scholz, F.; Vossmeier, T.; Schroedter, A.; Weller, H.; Yasuda, A. *J. Am. Chem. Soc.* **2004**, *126*, 3349.
- Beecher, P.; Quinn, A. J.; Shevchenko, E. V.; Weller, H.; Redmond, G. *J. Phys. Chem. B* **2004**, *108*, 9564.
- Beecher, P.; Quinn, A. J.; Shevchenko, E. V.; Weller, H.; Redmond, G. *Nano Lett.* **2004**, *4*, 1289.
- Chen, S.; Kimura, K. *Langmuir* **1999**, *15*, 1075.
- Chen, S. *Langmuir* **1999**, *15*, 7551.
- Zheng, W.; Maye, M. M.; Leibowitz, F. L.; Zhong, C.-J. *Analyst* **2000**, *125*, 17.
- Sinard, J.; Briggs, C.; Boal, A. K.; Rotello, V. M. *Chem. Commun.* **2000**, 1943.
- Chen, S. *J. Am. Chem. Soc.* **2000**, *122*, 7420.
- Templeton, A. C.; Zamborini, F. P.; Wuelfing, W. P.; Murray, R. W. *Langmuir* **2000**, *16*, 6682.
- Hicks, J. F.; Zamborini, F. P.; Osisek, A. J.; Murray, R. W. *J. Am. Chem. Soc.* **2001**, *123*, 7048.
- Zamborini, F. P.; Leopold, M. C.; Hicks, J. F.; Kulesza, P. J.; Malik, M. M.; Murray, R. W. *J. Am. Chem. Soc.* **2002**, *124*, 8958. Leopold, M. C.; Donkers, R. L.; Georganopoulou, D.; Fisher, M.; Zamborini, F. P.; Murray, R. W. *Faraday Discuss.* **2004**, *127*, 63.
- Shenar, R.; Rotello, V. M. *Acc. Chem. Res.* **2003**, *36*, 549.
- Daniel, M.-C.; Astruc, D. *Chem. Rev.* **2004**, *104*, 293.
- Adams, D. M. et al. *J. Phys. Chem. B* **2003**, *107*, 6668.
- Collins, P. G.; Bradeley, K.; Ishigami, M.; Zettl, A. *Science* **2000**, *287*, 1801.
- Kim, W.; Javey, A.; Vermesh, O.; Wang, Q.; Li, Y.; Dai, H. *Nano Lett.* **2003**, *3*, 193.
- Bradley, K.; Cumings, J.; Star, A.; Gabriel, J.-C. P.; Gruner, G. *Nano Lett.* **2003**, *3*, 639.
- Fuhrer, M. S.; Kim, B. M.; Dürkop, T.; Brintlinger, T. *Nano Lett.* **2002**, *2*, 755.
- Rosenblatt, S.; Yaish, Y.; Park, J.; Gore, J.; Sazonova, V.; McEuen, P. L. *Nano Lett.* **2002**, *2*, 869.
- Besteman, K.; Lee, J.; Wiertz, F. G. M.; Heering, H. A.; Dekker, C. *Nano Lett.* **2003**, *3*, 727.
- Duan, X.; Huang, Y.; Lieber, C. M. *Nano Lett.* **2002**, *2*, 487.
- Li, C.; Ly, J.; Lei, B.; Fan, W.; Zhang, D.; Han, J.; Meyyappan, M.; Thompson, M.; Zhou, C. *J. Phys. Chem. B* **2004**, *108*, 9646.
- Brust, M.; Walker, M.; Bethell, D.; Schiffrin, D. J.; Whyman, R. *J. Chem. Soc., Chem. Commun.* **1994**, 801.
- Parthasarathy, R.; Lin, X.-M.; Jaeger, H. M. *Phys. Rev. Lett.* **2001**, *87*, 186807.
- Bone, S.; Zaba, B. *Bioelectronics*; Wiley: Chichester, U.K., 1992.
- Wang, B.; Luo, J.; Wang, X.; Wang, H.; Hou, J. G. *Langmuir* **2004**, *20*, 5007.
- Abeles, B.; Sheng, P.; Coutts, M. D.; Arie, Y. *Adv. Phys.* **1975**, *24*, 407.
- Black, C. T.; Murray, C. B.; Sandstrom, R. L.; Sun, S. *Mater. Res. Soc. Symp. Proc.* **2001**, *D1071*, 636.
- Schroder, D. K. *Semiconductor Material and Device Characterization*; John Wiley & Sons: New York, 1991.
- Likharev, K. K. *Proc. IEEE* **1999**, *87*, 606 and references therein.
- Zhang, J. F.; Taylor, S.; Eccleston, W. *J. Appl. Phys.* **1992**, *71*, 725.
- Mean voltage sweep rate: $dV/dt|_{38K} \sim 500$ mV/s (see Figure 4a); $dV/dt|_{4K} \sim 75$ mV/s (see Figure 4b, Figure 4c)
- Snow, E. H.; Grove, A. S.; Deal, B. E.; Sah, C. T. *J. Appl. Phys.* **1965**, *36*, 1664.
- Vanheusden, K.; Warren, W. L.; Devine, R. A. B.; Fleetwood, D. M.; Schwank, J. R.; Shaneyfelt, M. R.; Winokur, P. S.; Lemnios, Z. *J. Nature* **1997**, *386*, 587.
- Jenkinson, R. I.; Ikram, A.; Horsewill, A. J.; Trommsdorff, H. P. *Chem. Phys.* **2003**, *294*, 95.